Measurement of nucleation site density, bubble departure diameter and frequency in pool boiling of water using high-speed infrared and optical cameras

Craig Gerardi, Jacopo Buongiorno*, Lin-wen Hu, Thomas McKrell

Massachusetts Institute of Technology
77 Massachusetts Ave., 24-206
Cambridge MA 02141, * 1 (617)253-7316 jacopo@mit.edu

ABSTRACT

A high-speed video and IR thermometry based technique has been used to obtain time and space resolved information on bubble nucleation and boiling heat transfer. This approach provides a fundamental and systematic method for investigating nucleate boiling in a very detailed fashion. Data on bubble departure diameter and frequency, growth and wait times, and nucleation site density are measured with relative ease. The data have been compared to the traditional decades-old and poorly-validated nucleate-boiling models and correlations. The agreement between the data and the models is relatively good. This study also shows that new insights into boiling heat transfer mechanisms can be obtained with the present technique. For example, our data and analysis suggest that a large contribution to bubble growth comes from heat transfer through the superheated liquid layer in addition to microlayer evaporation.

INTRODUCTION

Nucleate boiling is an effective mode of heat transfer; however, it is still relatively poorly understood. This gap stems from the decades-old difficulty of directly and accurately measuring important boiling parameters such as bubble departure diameter and frequency, bubble growth and wait times, and nucleation site density. To this date, very little data is available regarding time and space resolved bubble growth for nucleate pool boiling. The development of boiling studies on micro-scale heaters (Kim et al [1]; Myers et al [2]) and direct visualization of thermal patterns on a heated surface (T.G. Theofanous et al. [3]) have opened the doors to detailed experimentation and understanding of fundamental boiling physics. This study, which builds upon the aforementioned previous efforts, establishes a state-of-the-art experimental approach to measure bubble departure diameter and frequency, bubble growth and wait times, and nucleation site density in water pool boiling.

POOL BOILING FACILITY

A simple pool boiling configuration on a horizontal upward-facing flat plate was chosen. The experiments were operated at a uniform heat flux with a well-characterized, nano-film heating element.

A diagram of the facility used in this study is shown in Figure 1. A thin film made of Indium-Tin-Oxide (ITO) was directly heated. Boiling occurred on the upward facing side of this film which had an exposed area of 30x10 mm^2, and was 0.7 μm thick. The ITO was vacuum deposited onto a 0.4 mm thick sapphire substrate. This heater was connected to a DC power supply to control the heat flux at the surface. The cell accommodating the test fluid was sealed, included a condenser, and was surrounded by a constant-temperature water bath to maintain a constant test fluid temperature by minimizing heat losses to the ambient.

To acquire the temperature distribution on the heater surface, an infrared (IR) high-speed camera was used to measure IR intensity. Simultaneous high-speed video (HSV) was taken with a high-speed digital imaging system. A function generator produced a transistor-transistor logic (TTL) pulse at 480-500 Hz which triggered both cameras to simulataneously record an image allowing the synchronization of both cameras' image sequences.

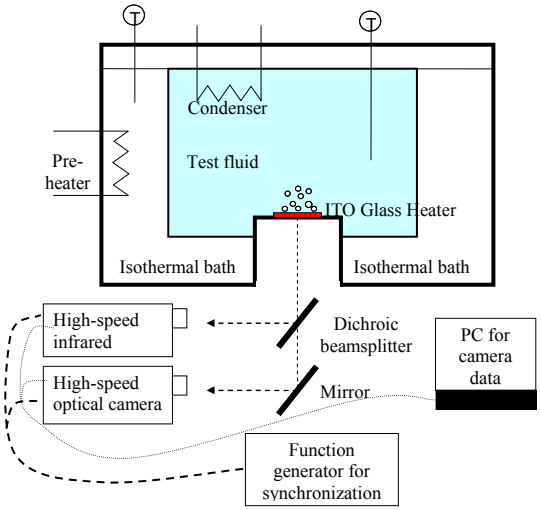

Figure 1: MIT pool boiling facility

A dichroic (hot-mirror) was placed directly below the heater which reflects the IR (3-5 μm) spectrum to the IR camera and transmits the visible (400-700 nm) spectrum. The visible spectrum is then reflected by a silver-coated mirror to the HSV system. Thus, both cameras image the area of interest from the same point of view. The sapphire substrate is transparent to both the IR and visible spectrums. The IR camera used was a SC 6000 from FLIR Systems, Inc. The HSV system was a Phantom v7.1 from Vision Research.

As configured in this study, the IR camera and HSV system had spatial resolutions of 100 μm and 50 μm respectively. In

the case of the IR image, this resolution is more than sufficient to capture the temperature history of individual bubble nucleation events at the nucleation sites since the typical nucleation site diameter is on the order of 1000μm. The frame rate of both cameras was 500 Hz.

Through calibration, IR intensity can be converted to temperature. The thinness of the ITO heater guarantees that the IR camera reading from its bottom is an accurate representation of the actual temperature on the top (wet side) of the heater surface. Use of the IR camera (vs. the more traditional approach based on thermocouples embedded at discrete positions in the heater) enables mapping of the complete two-dimensional time-dependent temperature distribution on the heater surface.

The heat flux was increased in discrete steps up to critical heat flux (CHF). At each intermediate step the temperature map and visualization were concurrently recorded for 1.0 sec. The test fluid was deionized (DI) water at atmospheric pressure and all experiments took place with the bulk temperature at the saturation temperature of water, T_{sat}=100 ˚C.

Heater characterization

The heating elements were characterized pre- and post-experiment in order to ensure a great deal of control and understanding over the surface properties. Both scanning electron microscopy (SEM) and confocal microscopy were used to analyze the heating elements after the experiments to show that there was little modification of the surface after boiling in DI water.

The surface roughness of the heater that has been boiled in DI water, as measured by the confocal microscope, was approximately the same as the as-received heater, SRa< 0.10 μm.

The value of the static contact angle, θ, for an unused heater is approximately 100°, while the contact angle of the heaters that were boiled in DI water only are 80-90°, suggesting that the boiling process alters the surface somewhat. The contact angle measurement error is within ±3°.

DATA REDUCTION AND UNCERTAINTY ANALYSIS

The raw infrared data obtained is a matrix of voltage values which is converted into temperatures via a calibration curve. These temperatures can by converted into a gray scale format in order to display the images shown in this paper. A custom graphical user interface (GUI) was created with MATLAB specifically for this work in order to manipulate and extract data. In order to understand the boiling process better, detailed information for each nucleation site at a given heat flux is desired. The process of finding and selecting nucleation sites was completed manually. Automated methods proved to be cumbersome and unreliable at properly determining the bubble departure diameter. These automation problems were compounded at high heat flux when bubbles interact and growth is asymmetric. The manual method consists of selecting the outer edge of each nucleation site, essentially drawing a line through its diameter. The outer edge is determined by the extreme change in temperature between a nucleation site and non-nucleating regions. The extreme change in contrast corresponds to a steep temperature gradient. A sample screenshot with a yellow line bisecting a single nucleation site is shown in Figure 2.

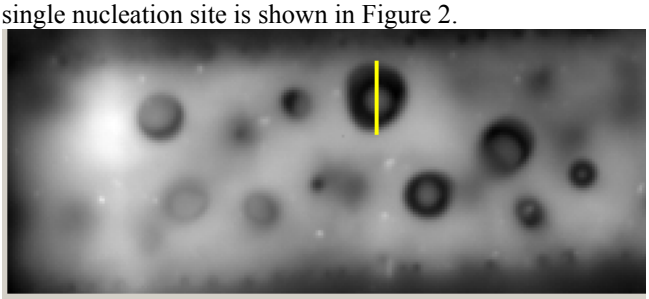

Figure 2: Sample screenshot of selecting the diameter of a nucleation site (yellow line bisects diameter). Nucleation sites appear as dark (cold) spots in IR images

Each frame is selected in sequence, and the nucleation events that have reached their peak diameter are selected. The center of each nucleation site is marked within the GUI in order to prevent double counting. In this way, every nucleation site is found along with the maximum diameter of each site. Example screenshots of the "selected" nucleation sites overlaying an IR screenshot of one frame for two different heat fluxes are shown in Figure 3.

It is important to note that due to the thinness of the ITO heater and substrate used in these experiments, along with the thermal properties of these materials, a nearly-perfect locally-constant surface heat flux boundary condition is obtained. A series of 3-D heat-conduction simulations were completed to confirm that at low heat flux (50 kW/m2) less than 10% of total heat generated in the ITO is conducted radially through the heater surface when a bubble forms on it, while at high heat flux (500 kW/m2) that fraction is < 2%. This is in contrast with traditional boiling experiments using a thick-copper-block-heater approach, which features a heater-averaged constant heat flux, but does have large local variations of the heat flux at the nucleation sites.

Nucleation site density

The nucleation site density can simply be found by taking the total number of nucleation sites and dividing by the total heated area. Since each site is selected manually, and every frame is examined to find nucleation sites, the uncertainty in this measurement is expected to be small, <2%.

Bubble departure diameter

The departure diameter of each bubble is logged via the method described above, and converted from pixel units to meters by multiplying by a conversion constant that is determined by using the known length of an imaged feature (the heater width and/or diameter).

The uncertainty in measuring the bubble departure diameter arises from three factors: accuracy of the distance calibration, measurement bias, and from not capturing the moment of departure. The total uncertainty is estimated to be of the order of 10% of the bubble departure diameter.

The diameter measured here is the bottom of the bubble that is in contact with the heater surface. The actual bubble departure size is typically larger (see Gerardi et al. [4]).

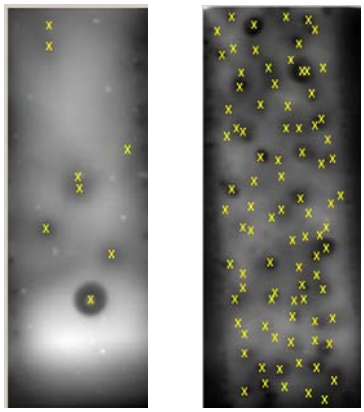

(a) (b)

Figure 3: Sample screenshots of nucleation site locations for DI Water (08_004) at (a) 50 kW/m^2 and (b) 500 kW/m^2

Bubble departure frequency

The bubble departure frequency for a given nucleation site is found by taking the inverse of the peak-to-peak time of the temperature response for the center pixel of each nucleation site, as shown in Figure 4. The average frequency for each nucleation site is chosen as the dominant frequency response for each site.

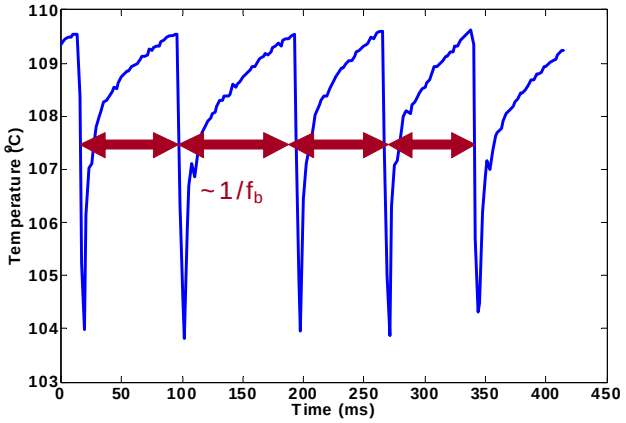

Figure 4: Temperature response of center pixel of a single nucleation site in DI Water (08_002) showing frequency response of nucleation cycle. Note the characteristic slow heating and sudden cooling cycles, which are expected during a bubble nucleation event.

The frequency measurement is automatically determined using the peak-to-peak times of the temperature response of each nucleation site. An individual peak-to-peak measurement could be off by a maximum of 2*1/fps≈4 ms, which accounts for initiation of bubble growth instantaneously after the previous frame was captured. At low heat flux (<100 kW/m^2) where the total cycle time is on the order of 80-220 ms, this error is insignificant. At high heat flux, the cycle time could be as low as 10 ms, meaning that this error would be significant for an individual cycle. However, a large number of repeated cycles are used to generate this average so the reported mean frequency should reflect the true frequency well. The distribution in cycle times (f_b=1/t_{cycle}) for an individual nucleation site at one heat flux (500 kW/m^2) is included in Figure 5. This figure shows that there is a fairly narrow distribution of cycle times for an individual nucleation site and it is approximately normally distributed about a mean value. This justifies the use of the mean value of the bubble frequency (or cycle time) at a given nucleation site for subsequent calculations. Similar behavior for all nucleation sites across all heat fluxes is observed.

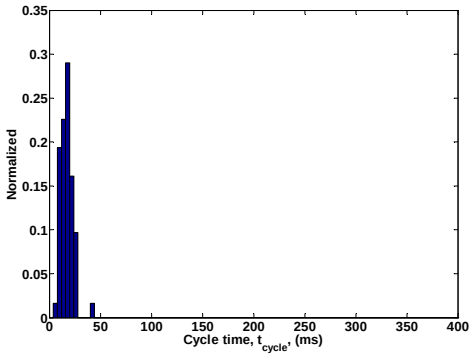

Figure 5: Single nucleation site for DI water test (08_006), q"=500kW/m^2 cycle time

Bubble growth time

The approximate bubble growth time is found by examining the derivative of the temperature response of the entire nucleation site. Plots of the average temperature of an entire nucleation site and its time derivative are shown in Figure 6. The start of bubble growth simply corresponds to the time at which the average temperature of the nucleation site begins to decline. The time at which bubble growth stops approximately corresponds to the time at which the time derivative of this average temperature equals zero. The difference in these two times is considered to be the bubble growth time as shown in the figure.

This automation method was benchmarked by manually inspecting the temperature response for several nucleation cycles at several sites. The growth times for each nucleation event are averaged for a single nucleation site in order to be tabulated and used for modeling.

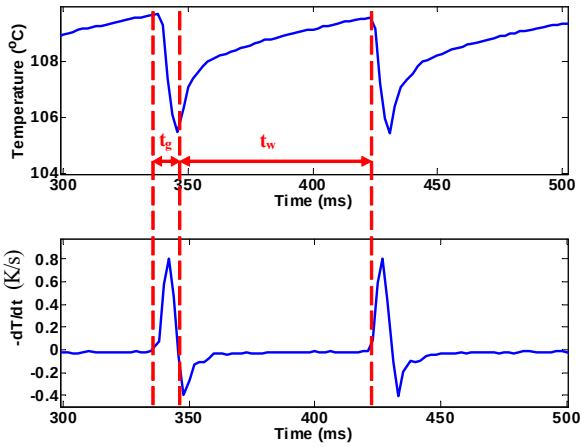

Figure 6: Average temperature of single nucleation site over time and the time derivative of this temperature response for DI Water (08_002). Growth and wait times are labeled

The uncertainty in the growth and wait time measurements could be as large as 4 ms which includes missing both the start and end of growth by approximately 1 frame. The wait time calculation is just the total cycle time minus the growth time. Like the average frequency, the growth and wait times

reported for each nucleation site are averaged over a large number of repeated cycles. Even though there is variability in the growth and wait times at a single nucleation site, the reported mean times should reflect the true times well due to the large number of data points.

The distribution in growth times for an individual nucleation site at one heat flux (500 kW/m^2) is included in Figure 7. This figure shows that there is a fairly narrow distribution of growth times for an individual nucleation site. This justifies the use of the mean value for the growth time at a given nucleation site for subsequent calculations. Note, that the data for a high heat flux is shown to highlight that while the growth time distribution is narrow, it is also banded by the measurement uncertainty.

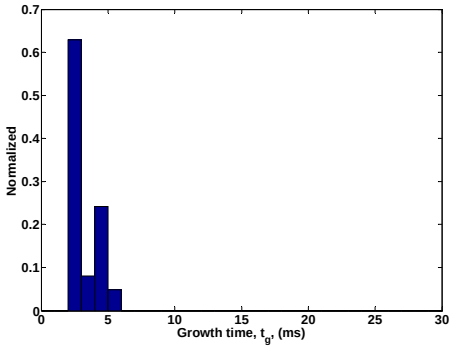

Figure 7: Single nucleation site for DI water test (08_006), q"=500kW/m^2 growth time

EXPERIMENTAL RESULTS

All data are for saturated deionized water boiling at P=1 atm (T_{bulk}=T_{sat}=100°C). A sample frame generated from the IR data at 100 kW/m^2 in DI water is shown in Figure 2. Light areas are warm (~109 °C), and dark areas are cooled nucleation sites. The uncertainty in the temperature measurements is estimated to be 2% or ~2°C.

Nucleate Boiling

At low heat flux nucleate boiling, where isolated bubble growth occurs, the growth cycle can be described as follows (Hsu & Graham, [5]). Once the liquid layer above the heater surface reaches the required surface superheat, ΔT_{sat}, to activate a given nucleation site a bubble begins to form which pushes the surrounding liquid outward. Evaporation occurs at the bubble interface and through the microlayer, which fuels further bubble growth.

A boiling curve is included in Figure 8 for the experimental run that is discussed in this work. This is generated by taking the average temperature for a ~5x5 mm^2 area in the center of the heater across a set (~1.0 s) of IR images for each heat flux shown. The boiling curve shows that the average heater wall temperature compares reasonably well with Rohsenhow's [6] prediction (C_{sf}=0.010). The critical heat flux (CHF) occurred between 900 and 1000 kW/m^2, which is approximately the Kutateladze-Zuber [7] prediction. The natural convection prediction of Fishenden & Saunders [8] is included as well.

A single representative bubble cycle is chosen from the synchronized experiments and the HSV and IR for this bubble are shown in Figure 9 and Figure 10 respectively. The HSV shown in Figure 9 visually depicts bubble growth. The depth of field for this particular camera setup is sufficient to see several millimeters past the heater surface, thus capturing the shape and size of the bubble even as it detaches from the heater surface. The outer radius of the bubble, R_t, and the microlayer radius, r_c, are clearly visible in these images. Both the hemispherical radius and dry out radius are assumed from the IR data as shown in Figure 10. The hemispherical radius is taken to be the cooled (thus dark colored) circular expanding area. The dry out area is taken to be the hotter (thus light colored) circular area that expands in the center of the cooled area.

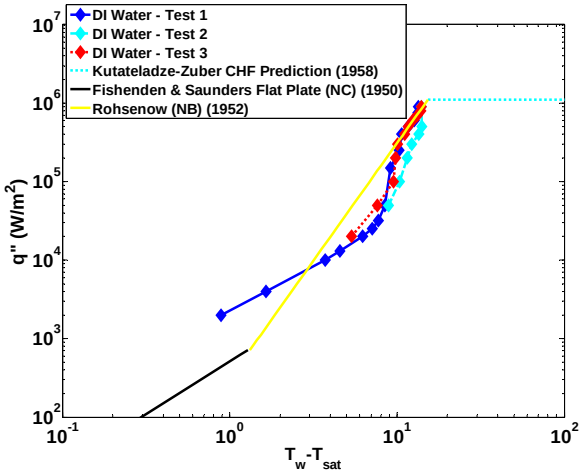

Figure 8: Boiling curve for pure DI water. Experimental results compared to various models

After bubble departure (~ frame 55), cool liquid rushes in to replace the space previously occupied by the bubble. The layer of liquid that is now immediately above the heater surface is gradually heated by transient conduction until it again reaches the required superheat to spawn a new bubble after which the bubble growth process repeats. The time between bubble departure and new bubble growth is called the waiting period, t_w.

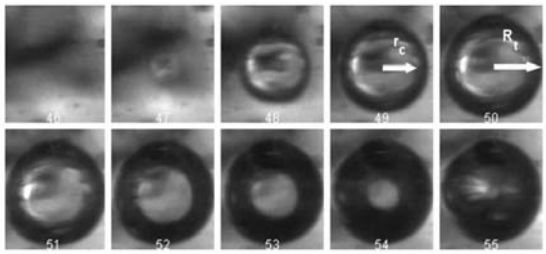

Figure 9: HSV for a single bubble life-cycle for frames 46-55 in DI water at 60kW/m^2. Time interval between consecutive images is ~2.08ms (08_002).

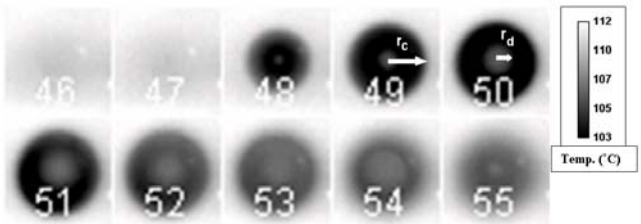

Figure 10: IR data for a single bubble life-cycle for frames 46-55 in DI water at 60kW/m^2. Time interval between consecutive images is ~2.08ms (08_002).

Initial hemispherical growth is supported with the HSV of Figure 10. Frame 48 shows that the outer bubble radius, R_t, and the hemispherical radius, r_c, have approximately the same value, suggesting that the initial bubble growth is primarily in the radial direction along the surface. Contrast this with later frames (49-51), where the outer bubble radius is significantly larger than the hemispherical radius.

Previous work by the present authors (Gerardi et al. [4]) used these synchronized sets of bubble growth images to confirm the existence of microlayer evaporation in water.

Measured and equivalent diameter

Assuming that all heat transferred from the wall is used as latent heat, an equivalent bubble radius (d_{evap}) can be computed as:

$$\rho_v \frac{\pi d_{evap}^3(t) h_{fg}}{6} = \int_0^t q''(t) A_{heated} dt \qquad (1)$$

Where t=0 is assumed to be the start of nucleation for a single bubble. Thus the equivalent bubble radius, R_{evap}, can be evaluated as

$$R_{evap}(t) = \frac{1}{2} d_{evap}(t) = \frac{1}{2}\left(\frac{6}{\pi \rho_v h_{fg}} \int_0^t q''(t) A_{heated} dt \right)^{1/3} \qquad (2)$$

With A_{heated} being the footprint of the bubble at any time, t, taken from the measured bubble radius using the HSV data.

The measured bubble radius from the HSV is compared with the computed equivalent radius in Figure 11 at q"=60 kW/m^2 in DI water. Measured bubble radius data averages 5 bubbles with the error bars representing the minimum and maximum measured values. The equivalent evaporation bubble radius. .The well-known Mikic [9] prediction is included in this figure as well. The equivalent radius represents an upper bound on the heat that can be directly transferred from the wall to the bubble during its growth stage.

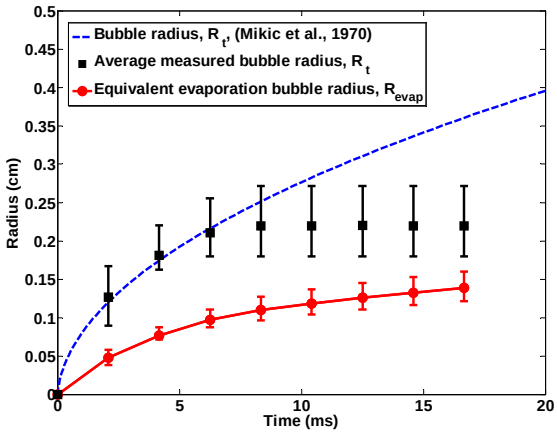

Figure 11: Comparison of the measured radius, R_t, (taken from HSV) to the equivalent radius, R_{evap}, q"=60 kW/m^2 in DI water (08_002). Measured diameter error is within ±10%.

The figure clearly shows that the computed equivalent radius is significantly smaller than the measured radius. This is strong evidence that the bubble gains a significant amount of the energy required for it to grow from the superheated liquid layer as opposed to the traditional hypothesis that bubble growth is driven by microlayer evaporation fuelled by direct heating from the wall. Instead, it seems that the superheated liquid layer acts as a capacitor, storing energy for the bubble to siphon off during growth. This energy is replenished via conduction and micro-convection during and following bubble growth. This finding is consistent with experiments using subcooled FC-72 as the working fluid by Yaddanapuddi and Kim [10] and Demiray and Kim [11] & [12], who used microheaters that locally controlled the surface superheat while measuring the local heat flux, in contrast with our approach which controls the heat flux while measuring the local temperature. Interestingly, both approaches arrive at the same conclusion.

Measured bubble parameters

A summary of the bubble parameters (D_b, NSD, f_b, t_g, t_w) discussed above are presented here in Figure 12 through Figure 16. Each data point in these figures represents the average values of all the nucleation site average bubble parameter values at a given heat flux over 5x5 mm^2 area in the center of the heater. For example, the average value of the growth time of the single nucleation site shown in Figure 7 is combined with the average values of every other nucleation site growth times at that heat flux and then presented as a single data point in Figure 15.

The bubble departure sizes versus wall superheat are presented in Figure 12 along with two theoretical models, Zuber [13] and Jensen & Memmel [14]. The often-cited Fritz [15] model drastically overpredicts the measured departure diameters, giving a value of 4.7 mm for all superheats assuming θ=90° (not shown in figure). There is some variation in the data, especially in test 08_004 at low heat flux. However, the data are in the range predicted by the models.

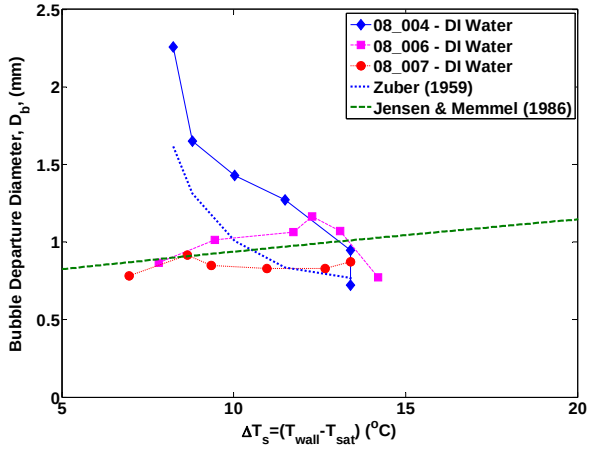

Figure 12: Measured bubble departure diameters vs. wall superheat compared with several theoretical models

The measured nucleation site densities versus wall superheat are presented in Figure 13 along with two theoretical models. The measured trend of increasing nucleation site density with increasing wall superheat is

exhibited in both models. The measured data agree relatively well with the Wang and Dhir [16] model with θ=90°. The Kocamustafaogullari and Ishii [17] prediction for θ=90° is included for reference, and under predicts the nucleation site density data.

The measured bubble departure frequencies versus wall superheat are presented in Figure 14.

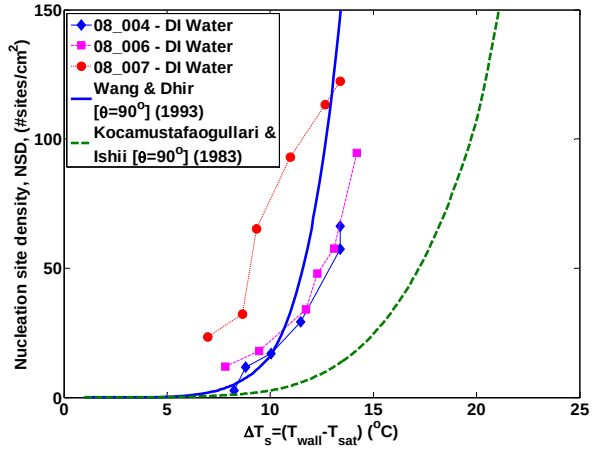

Figure 13: Measured nucleation site densities vs. wall superheat compared with two theoretical models

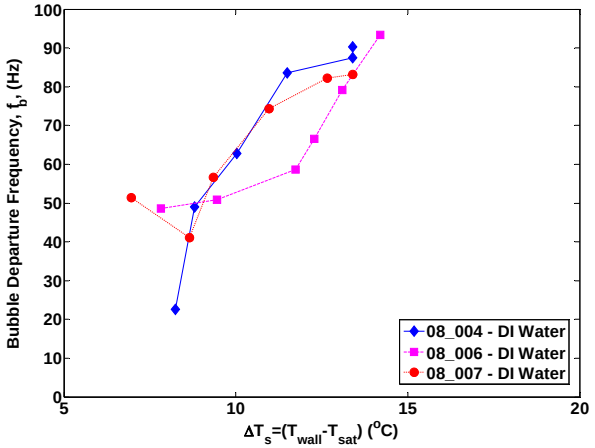

Figure 14: Measured bubble departure frequencies vs. wall superheat

The measured bubble growth times versus wall superheat are presented in Figure 15 along with the Hatton and Hall [18] model. The data and model are of the same order, while the slight discrepancy could be attributed to the large growth time measurement uncertainty.

The measured bubble wait times versus wall superheat are presented in Figure 16 along with the Han and Griffith [19] model. Their model predicts the minimum wait time, while their experimental data was between 17 and 130 times the model's minimum. Thus, the model is arbitrarily multiplied by a factor of 40 in Figure 16 in order to show that the trend predicted by the model matches well with the present data.

As mentioned previously, the ratio of growth time to cycle time is an important parameter in most theoretical models, and is thus plotted in Figure 17 along with the van Stralen [20] value of 0.25. The present data is the first time that this ratio is found experimentally for a wide range of superheats. It is quite clear that while the van Stralen value matches the data at high superheat, the model clearly overpredicts it at low superheat.

Lastly, the measured bubble departure frequencies vs. their corresponding measured bubble departure diameters are shown in Figure 18 along with the theoretical models of Jakob & Fritz [21], Zuber [13], and Cole [22]. There is reasonable agreement between the data and models.

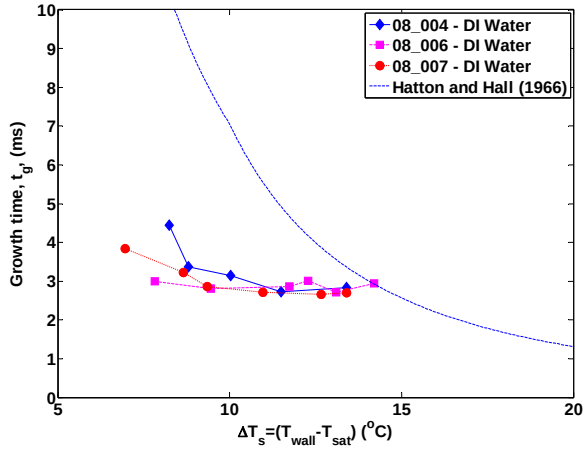

Figure 15: Measured bubble growth times vs. wall superheat compared with the Hatton and Hall (1966) model

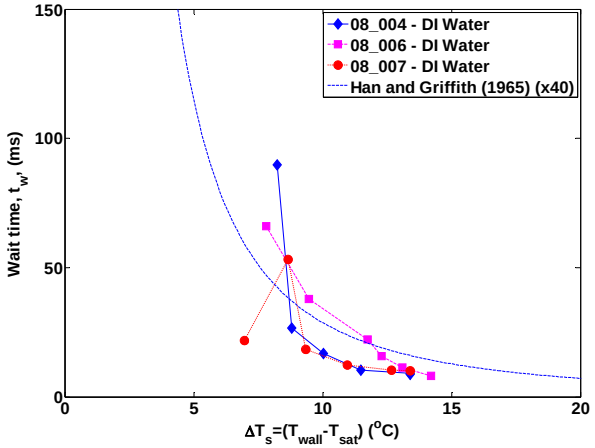

Figure 16: Measured bubble wait times vs. wall superheat compared with the Han and Griffith (1965) model

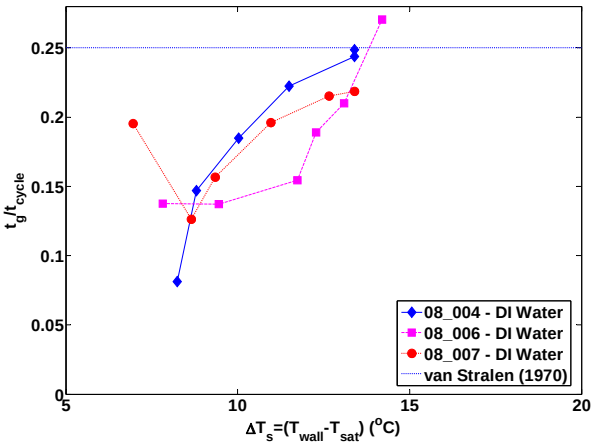

Figure 17: Measured growth time to cycle time ratio vs. wall superheat compared with van Stralen's (1970) value of 0.25

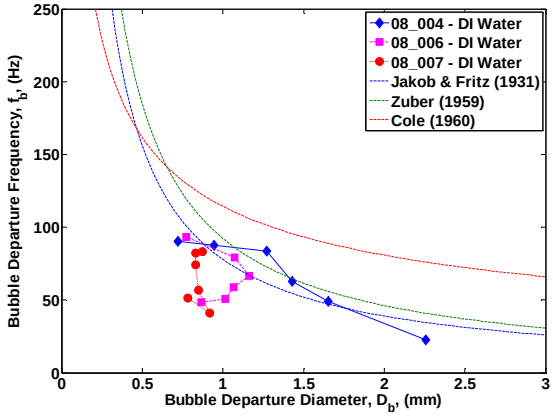

Figure 18: Measured bubble departure frequencies vs. measured bubble departure diameters compared with several theoretical models

Nucleate boiling heat transfer coefficient

One of the most prominent techniques of predicting the nucleate boiling heat transfer coefficient from basic principles is called heat flux partitioning (Kurul & Podowski [23]), which has also been labeled as the "RPI Model" after the authors' university. The model is based on the Bowring [24] scheme of accounting for the various boiling mechanisms separately. Both have primarily been developed for flow boiling, but have been extended to pool boiling here. This model requires knowledge of the bubble parameters discussed in the sections above. Therefore, in this section, starting from the bubble parameter input, we test the model's ability to predict the boiling curve.

According to the RPI model, the heat removed from the heating surface by boiling liquid is assumed to be by the following mechanisms:

i. the net heat to form the vapor phase (q_e)
ii. heat expended in re-formation of the thermal boundary layer, or the so-called quenching heat flux (q_q)
iii. heat transferred to the liquid phase outside the zone of influence of the bubbles by turbulent natural convection (q_c).

The total boiling heat flux is obtained through the addition of the three fluxes as:

$$q''_{tot} = q''_e + q''_q + q''_c . \qquad (3)$$

Since the present work has obtained detailed information for the bubble parameters, it is possible to write expressions for the partitioned heat fluxes that incorporate the incremental contributions of each nucleation site.

Assuming that all of the energy transferred from the heater area below an individual bubble during growth is in the form of latent heat, the total evaporative heat flux can be written as

$$q''_e = \frac{\pi}{6A}\rho_g h_{fg} \sum_{n=1}^{N_T} \left(f_{b,n} \bullet D_{b,n}^3 \right) \qquad (4)$$

where N_T is the total number of nucleation sites.

Using the Han and Griffith [19] assumption that as a bubble departs, it carries an area of the superheated thermal boundary layer with it in its wake equal to twice the bubble diameter, and that this cool liquid is heated via transient conduction from the heater, the total quench heat flux is given as:

$$q''_q = \frac{2\pi k_l (T_w - T_{sat})}{A\sqrt{\pi \alpha_l}} \sum_{n=1}^{N_T} \left(D_{b,n}^2 \left(\sqrt{t_{w,n}\, f_{b,n}} \right) \right) \qquad (5)$$

The McAdams [25] estimate for the turbulent natural convection heat transfer coefficient from a flat upwards-facing plate is used to estimate the total natural convection heat flux as:

$$q_c = \left[1 - \frac{\pi}{4A} \sum_{n=1}^{N_T} \left(D_{b,n} \right)^2 \right] h_{turb} \left(T_w - T_{sat} \right) \qquad (6)$$

The boiling curve for one experiment (08_007) is shown in Figure 19 along with the evaporation, quench, convection and total partitioned heat fluxes that have been calculated using the method described above. The model works surprisingly well when considering the amount of independent data that has been fed into it. It is also interesting to note that the quench heat flux is the dominant partitioned heat flux, and not the evaporative heat flux, as one may expect. This further supports the conclusion made earlier that the superheated liquid layer is responsible for the majority of the surface heat removal, and not direct surface-to-bubble latent heat transfer.

The total partitioned heat fluxes for the three experiments analyzed in this work are presented in Figure 20, and all exhibit approximately the same behavior.

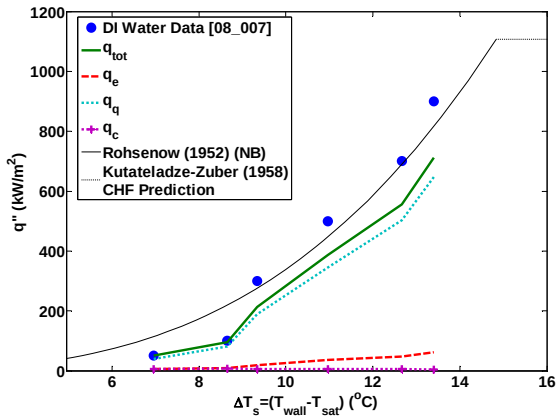

Figure 19: Comparison of actual boiling curve (●) with RPI partitioning model using corresponding bubble parameters (D_b, NSD, f_b, t_g, t_w) for each superheat. DI Water test (08_007)

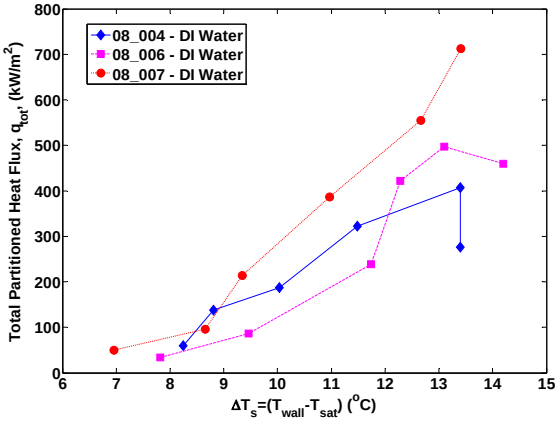

Figure 20: Total partitioned heat flux boiling curve, q_{tot}, as predicted by RPI model using current data as bubble parameter inputs

CONCLUSION

A high-speed video and IR-thermometry-based technique has been used to obtain time and space resolved information on bubble nucleation and boiling heat transfer. This approach provides a fundamental and systematic method for investigating nucleate boiling in a very detailed fashion. Data on bubble departure diameter and frequency, growth and wait times, and nucleation site density are effortlessly measured. The data have been compared to decades-old and poorly validated models and correlations. The agreement between the data and the models is generally reasonable.

New insights into boiling heat transfer mechanisms have also been obtained. For example, our data and analysis suggest that bubble growth is significantly fueled via heat transfer through the superheated liquid layer in addition to the direct heat supply from the heater surface. This confirms for water previous observations that were obtained for FC-72.

NOMENCLATURE

A	area [m^2]
d	diameter [m]
D_b	bubble departure diameter [m]
f_b	bubble departure frequency [Hz]
fps	frames per second [Hz]
h	heat transfer coefficient
h_{fg}	latent heat of vaporization [kJ/kg]
k	thermal conductivity [W/m k]
NSD	nucleation site density [# sites/cm^2]
N_T	total nucleation number [#]
P	pressure [atm]
q"	heat flux [kW/m^2]
R	radius [m]
r_c	hemispherical radius [m]
R_t	outer bubble radius [m]
T	temperature [°C]
t	time [sec]

Greek

α	thermal diffusivity [m^2/s]
θ	contact angle [degrees]
ρ	density [kg/m^3]

Subscript

bulk	bulk
c	convective partitioned
cycle	ebullition cycle (growth + wait)
e	evaporative partitioned
g	growth
heated	heated
l	liquid
n	nucleation site number
q	quench partitioned
s	superheat
sat	saturated
turb	turbulent natural convection
w	wait
wall	wall

REFERENCES

[1] J. Kim, C.P. Ch'ng, and T.S. Kalkur, (1996) "Design of An Improved Heater Array to Measure Microscale Wall Heat Transfer", 3rd Microgravity Fluid Phys Conf, NASA Conf Pub, 3338, June, pp. 165-170

[2] J.G. Myers, V.K Yerramilli, S.W. Hussey, G.F. Yee, J. Kim (2005), "Time and space resolved wall temperature and heat flux measurements during nucleate boiling with constant heat flux boundary conditions," Int. J. Heat Mass Trans, **48**, pp 2429-2442

[3] T.G. Theofanous, J.P. Tu, A.T. Dinh and T.N. Dinh, (2002), "The Boiling Crisis Phenomenon", J. Experimental Thermal Fluid Science, P.I:pp. 775-792, P.II: pp. 793-810, **26** (6-7)

[4] C. Gerardi, J. Buongiorno, L.W. Hu, T. McKrell, (2008), "Experimental observation of the dynamic micro- and macro-layer during pool boiling," Proceedings of the 2008 ASME Heat Transf, Fluids, Energy & Energy Nano Conf, Jacksonville FL

[5] Y.Y Hsu, R.W. Graham, (1986), "Transport Processes in Boiling and Two-Phase Systems", American Nuc Soc, Inc., Illinois, USA

[6] W.M. Rohsenow, (1952), "A method of correlating heat transfer data for surface boiling of liquids," Trans. ASME, **74**, 969-975

[7] N. Zuber, (1958), "On the stability of boiling heat transfer," Trans. ASME J. Heat Transfer, **8** (3), pp. 711-720.

[8] M. Fishenden, O. Saunders (1950), An Introduction to Heat Transfer, Oxford University Press

[9] B.B. Mikic, W.M. Rohsenhow, P. Griffith, (1970), "On Bubble Growth Rates", Int. J. Heat Mass Transf, **13**, pp. 657-666.

[10] N. Yaddanapudi, J. Kim, (2001), "Single bubble heat transfer in saturated pool boiling of FC-72," Multiphase Sci. Technol, **12**(3-4), 47-63

[11] F. Demiray, J. Kim, (2002), "Heat transfer from a single nucleation site during saturated pool boiling of FC-72 using an array of 100 micron heaters," Proc 2002 AIAA/ASME Joint Thermophysics Conf, St. Louis, MO

[12] F. Demiray, J. Kim, (2004), "Microscale heat transfer measurements during pool boiling of FC-72: effect of subcooling," Int J. Heat Mass Transfer, **47**, 3257-3268

[13] N. Zuber (1959), "Hydrodynamic aspects of boiling heat transfer," U.S. AEC Report AECU 4439, June

[14] M.K. Jensen, G.J. Memmel, (1986), "Evaluation of bubble departure diameter correlations," Proc Eighth Int. Heat Transf. Conf., **4**, pp. 1907-1912

[15] W. Fritz, (1935), "Berechnung des Maximalvolume von Dampfblasen, Phys. Z., **36**, pp 379-388

[16] C.H. Wang, V.K. Dhir (1993a), "Effect of surface wettability on active nucleation site density during pool boiling of water on a vertical surface," ASME J of Heat Transf, **115**, pp 659-669

[17] G. Kocamustafaogullari, M. Ishii, (1983), "Interfacial area and nucleation site density in boiling systems," Int. J. Heat Mass Transfer **26**:1377–1387

[18] A.P. Hatton, I.S. Hall, (1966) "Photographic study of boiling on prepared surfaces," Third International Heat Transfer Conf., **4**, Chicago, IL, August 7-12, pp. 24-37

[19] C.Y. Han and P. Griffith, (1965) "The mechanism of heat transfer in nucleate pool boiling – I and II," Int. J. Heat Mass Transfer, 8, 887-914

[20] S.J.D. van Stralen, (1970), "The boiling paradox in binary liquid mixtures," Chem. Eng. Sci, **25**, pp 149-171

[21] M. Jakob, W. Fritz, (1931), "Versuche uber den Verdampfungsvorgang," Forsch. Ingenieurwes, **2**, pp. 435-447

[22] R. Cole, (1960), "Photographic study of boiling in region of critical heat flux," AIChE Journal, **6**, pp. 533-542

[23] N. Kurul, M.Z. Podowski, (1990), "Multidimensional effects in forced convection subcooled boiling", Proc. 9th Int Heat Transf Conf, Jerusalem, Israel. pp. 21-25

[24] R.W. Bowring (1962), "Physical model based on bubble detachment and calculation of steam voidage in the subcooled region of a heated channel," OECD Halden Reactor Project Report HPR-10

[25] W.H. McAdams, (1945) *Heat Transmission* (3rd Ed), p. 180, McGraw-Hill, New York.